Automated Microscopy and Particle Size Analysis of Dynamic Fragmentation in Natural Ceramics

James D. Hogan[a,b], Josemar A. Castillo[c], Alan Rawle[c], John G. Spray[b], Robert J. Rogers[a]

[a]*Department of Mechanical Engineering, University of New Brunswick, Fredericton, New Brunswick E3B 5A3, Canada*
[b]*Planetary and Space Science Centre, University of New Brunswick, Fredericton, New Brunswick E3B 5A3, Canada*
[c]*Malvern Instruments Inc., 117 Flanders Road, Westborough, MA, USA*

Abstract

The dynamic fragmentation of gabbro and granitoid tiles, and coarser and finer grained granitoid blocks have been examined for impact energies of 21 J to 3,040 J. Intra-grain fragmentation and inter-granular frictional melting were observed to be common features of the fragmentation process. Consideration of analytical models indicate these temperatures are achievable under these moderate impact conditions.

Median values of the number-based sub-10 μm fines, and the number- and volume-based 10 μm to 2 mm fragments were compared with existing theoretical models predicting dominant fragment size. The simplistic model proposed by Grady predicts reasonably well the median fragment size for the volume-based distribution. More complex models are able to predict reasonably well median values for Q_0. Ultra-fine production was not predictable. These results suggest there are two distinct fragment-forming mechanism during impact testing of nat-

Email address: jd.hogan@unb.ca (James D. Hogan)

ural materials. One mechanism is based on energy consideration of the bulk material, which produces the larger fragment size, and the other is associated with micro-scale comminution, which produces sub-10 μm fines.

Keywords: fragment morphology characterization, dynamic fragmentation of natural ceramics, impact testing, railgun, particle size analysis, fractal dimension

1. Introduction

Comminution is the process of particle-size reduction through crushing or grinding. It is energy-intensive and results from the interaction of poorly understood micro-scale friction, fracture, and plastic deformation processes. During comminution, particle fracture initiates at pre-existing flaws and propagates in response to local tensile stress components acting normal to the crack plane [1]. Local tensile stresses are commonly generated even when the external loading is predominantly compressive [1]. The nature of the stress field and material properties govern the size and shape distribution of comminuted fragments [1]. For rocks and minerals, important material properties include the yield and shear yield strength, fracture toughness, and thermal conductivity. Minerals with lower fracture toughness and melting temperatures are preferentially comminuted [2]. Understanding the role of particle-size reduction (i.e., fragmentation) is important in seismology and earthquake science [3], volcanology [4], and, more fundamentally, the dynamic fracture and fragmentation of brittle materials. The fragmentation of natural ceramics is examined in this paper.

The reduction of particle sizes via comminution is energy intensive [5], with efficiencies [1] of $\sim$1% to $\sim$2% [5, 7, 8]. Higher efficiencies ($\sim$ 15%) are estimated

[1] defined as the relation of mechanical strain energy input to the fracture surface area energy

when the energy required for single particle fracture is considered instead of the energy required for creating new surface area [6]. The study of energy conversion and efficiencies continues to remain a widely studied topic in comminution studies, where it is assumed that minor improvements in understanding, technology and techniques can lead to substantial improvements in industrial processing efficiences.

A critical size for comminuted fragments has been observed below which no further fragmentation occurs [9, 10]. This is know as the comminution, or grinding, limit and has been studied by many authors [9–12]. The comminution limit is achieved when the particle size is so small that no further defects can be stored in the lattice [13]. It is dependent on loading conditions and material properties [13], temperature, and strain rate. Below this size, fragments flow plastically and alter their shape rather than undergo further fragmentation [9, 10]. The change of fracture to plastic flow results in a large increase in material strain (from 0.1-0.3 $\%$ up to 30-100$\%$ [12]), resulting in a significant increase in particle strength due to strain hardening [14].

This paper explores the dynamic fragmentation of natural ceramic granitoid and gabbro tiles (10 mm thick), and fine and coarser grained granitoid blocks (55 mm thick). Fragment distributions based on number and volume considerations are determined using gravity-feed and automated microscopy particle sizing techniques. These are compared with existing analytical models. Physical consequences of dynamic fracture are explored using scanning electron microscopy. The effect of experimental conditions is considered and implications.

---

generated [6]

2. Experimental Setup and Analysis Methods

The impact tests were performed at the French-German Research Institute of Saint-Louis (ISL), France, to investigate the dynamic fracture of natural ceramic materials. The SR 3/60 electromagnetic railgun was used as the launching platform. Materials include: fine (Figure 1a) and coarse grained (Figure 1b) granitoid blocks (55 mm in thickness), and gabbro (Figure 1c) and fine grained (Figure 1d) granitoid tiles (10 mm in thickness). Aluminum (left in Figure 1e) (65 g) projectiles were used in the tiles and coarser-grained block experiments. Composite (right in Figure 1e) (45 g) projectiles were used for the finer grained granitoid block experiments. Impact energies ranged 21 J (26 m/s) to 305 J (100 m/s) for the gabbro tiles, 716 J (152 m/s) to 1,790 J (240 m/s) for the granitoid tiles, 2,710 J (347 m/s) to 6,810 J (550 m/s) for the finer grained granitoid blocks, and 1,940 J (250 m/s) to 3,040 J (313 m/s) for the coarser grained granitoid blocks. Fragments were collected, sized and counted at Malvern Instruments, Westborough, MA using a Parsum IP 70-S gravity-feed probe [15] with an operating range of 10 μm to 6 mm. Secondary electron (SE) and back-scattered electron (BSE) images of the fracture surfaces were obtained using a Hitachi SU-70 analytical Field Emission Scanning Electron Microscope (FESEM).

The Morphologi G3 [16] system was used to characterize the size and shape of the smaller particulates for the highest impact energy cases for each of the four materials. Specimens were obtained from the samples by sieving in order to remove particles larger than 200 μm. Approximately 20 mm^3 of the sieved samples were dispersed using the integrated sample dispersion unit (SDU) [16]. This software-controlled unit allows for precise and reproducible dispersion of dry particles by applying an instantaneous pulse of compressed air to the sample,

which is encapsulated by two foil membranes within the SDU cartridge. In this analysis, the dispersion was optimized using a pressure of 0.8 bar and 6 μm carrier foils. Automated microscopy is an optical counting method. The microscope stage is translated across the dispersed sample, images are collected, and the G3 software identifies fragment sizes and shapes. Fragments with an area less than 100 pixels were removed to ensure adequate shape comparison.

3. Results

Post-impact features of the targets (Figure 2) are initially investigated. Analysis of the target rear for the finer grained granitoid at 3,730 J (Figure 2a) and the gabbro tile at 305 J (Figure 2d) reveal the formation of cones, initiating at the front surface and expanding through to the rear of the target, within the material. Circumferential and radial through-cracking is also observed for the gabbro tiles (Figure 2c). Similar features as in the gabbro tiles are observed for the granitoid tiles (not shown). No observable cones are present in the coarser grained block at 3,040 J (Figure 2b).

Shown in Figure 3a is the ratio of collected mass of fragments $<$ 16 mm to the original mass of the target. The fragments $<$ 16 mm are referred to as the 'collected mass'. The ratio of mass increases as the impact energy is increased over this range according to according to $0.017x^{0.53}$ for the gabbro tile, $0.026x^{0.34}$ for the granitoid tiles, 8E-4$x^{0.83}$ for the larger grained granitoid, and 19E-3$x^{0.42}$ for the finer granitoid material (Figure 3a). Higher energies and those experiments involving blocks produce more $\%$ of mass. In addition, the rate of increase for mass is greatest for the largest-grained material (black granitoid block) and decreases in rate with decreasing grain size (gabbro, finer-grained granitoid block,

and granitoid tile).

Shown in Figure 3b is the relationship between the number of fragments and the impact energy. There is a greater rate of increase for the coarser grained granitoid blocks (609E3$x^{0.67}$) and the gabbro tiles (7.88$x^{1.28}$) than for the granitoid tiles (15E3$x^{0.12}$) and finer grained granitoid blocks (75E3$x^{0.11}$). As a result of slower rate of increase, finer grained materials have greater proportionality constants.

Shown in Figure 3c are trends in the 10^{th} (x_{10}), 50^{th} (x_{50}) and 90^{th} (x_{90}) percentiles for the number distribution (Q_0) of fragments. Note the logarithmic axes. These values are a measures of the finer material (x_{10}), central/median material (x_{50}) and larger material (x_{90}) in the sample. These are recommended per ISO 9276-2:2001 [17] standards and, combined, they are used to better understand the fragmentation processes. Corresponding linear fits of the data are also shown in the figure. Slopes are in the order of $x_{90}>x_{50}>x_{10}$ and are greater for the tile experiments than the block experiments.

Kick [18], on the other hand, concluded that energy is proportional to volume or weight for mm-size processes (e.g., crushing, fragmentation during impact testing). For this reason, investigation of volume distributions (length^3 $\times$ number) are important as they represent the length scale indicative of fracture energy dissipation. The volume distribution is the contribution of total volume at each length scale. Values of x_{10}, x_{50}, and x_{90} are explored for the volume distribution (Q_3) of fragment size (Figure 3d). Again, slopes are $x_{90}>x_{50}>x_{10}$, indicating that one additional unit of energy causes a greater reduction in particle size for larger particles than smaller ones. The tile experiments are also more sensitive (i.e., greater slopes) to an increase in impact energy than than the block experiments. There are also more fines in the finer grained granitoid tile and block experiments. Within

the tile (gabbro vs. granitoid) and block (coarser vs. finer) groups, coarser grained materials are more sensitive to input energy and have larger values of x_{10}, x_{50}, and x_{90}.

Characteristics of fragment size and circularity ($2\times\sqrt{\pi \times Area}/perimeter$) are examined in greater detail in Figure 4 for the highest energy cases for each material. Shown in Figure 4a are distributions of fragment size for all materials. Automated microscopy is a different measurements technique than the Parsum and, thus, should be considered separately. The lower limit for the Parsum probe measurements is indicated on Figure 4a. Total fragment numbers of 18,923 for the gabbro tiles, 25,032 for the granitoid tiles, 31,794 for the coarser block and 52,933 for the finer block reflect the significant contribution of the finer fragments to the number distribution of particle sizes; something that was not entirely captured due to the >10 μm limit of the Parsum probe. Measurements of the sub-200 μm fragments are investigated here to gain a better understanding of fragmentation mechanisms associated with the different experimental conditions.

Distributions for both tiles are bi-modal with peaks at sub-10 μm and approximately 120 μm (Figure 4a). Larger peaks are in the order of median values in Parsum probe measurements (Figure 3c). Both peaks are a product of the limits (lower of $\sim$2 μm and upper of $\sim$1,000 μm) of the instrument. The distribution for the coarser block material has a peak value at 35 μm, while the distribution for finer grained granitoid is skewed towards the finer scales with a sub-10 μm peak. The bulk of the distributions for the gabbro and granitoid tiles and the finer grained block contain sub-10 μm fragments (smaller than the Parsum measurements).

Corresponding values of x_{10}, x_{50}, and x_{90} for fragment sizes are shown in Figure 4b. Considerably more fines are contained in the gabbro (x_{10GAB}=3.5 μm)

and granitoid (x_{10GT}=3.2 μm) tiles and the finer grained block (x_{10FG}=3.5 μm) than the coarser block (x_{10LG}=7.9 μm). Increased grinding, especially for the finer grained granitoid tile and block, is also observed in median values (x_{50GAB}=8.7 μm, x_{50GT}=6.2 μm, x_{50FG}=6.7 μm, and x_{50LG}=35.0 μm). Values of x_{90GAB}=201.0 μm, x_{90GT}=151.1 μm, x_{90FG}=31.2 μm, and x_{90LG}=116.8 μm further highlights characteristics of distributions observed in Figure 4a. In particular, the bi-modal peak $>$100 μm represents more of the population for the gabbro material than the granitoid tile.

Shown in Figure 4c are distributions of fragment circularity. Corresponding values of x_{10}, x_{50}, and x_{90} are shown in Figure 4d. As references, circles have circularlity=1, squares have a circularlity=0.89, and ellipsoids (with one axis twice as long as the other) have a circularlity=0.89. Distributions for the finer grained granitoid tile and block are more skewed towards unity, indicating they are more circular in morphology. Median values of x_{50GAB}=0.90, x_{50GT}=0.93, x_{50FG}=0.94, and x_{50LG}= 0.87 reflect higher circularity for the granitoid tile and the finer grained granitoid block.

4. Evaluation of Fragmentation Mechanisms using Scanning Electron Microscopy

Physical features of the fragmentation process are examined using scanning electron microscopy in Figure 5. Examples of fracture surfaces for the finer grained granitoid block and the gabbro tile are shown in Figure 5a and b, respectively. Inter-granular fracture is common in the granitoid block. Roughened surfaces promote sub-fine production (also observed on the surface). A more detailed analysis of fracture surfaces and energy dissipation mechanisms in the finer

grained granitoid block is published in Hogan et al. [19]. Fracture commonly occurs along grain boundaries in the coarser block, with much less fine production occurring (not shown). Fracture surfaces in the gabbro tile are rough, suggesting that inter-granular rupture was the primary mechanism of fragmentation (Figure 5b). Rupture is a result of the rapid deformation of the rock from the transfer of energy and momentum directly from projectile contact. Rupture of the target is assumed over other mechanisms due to thin target thickness. This feature is also a common in the granitoid tiles.

Intra-fragment features for the finer grained granitoid block are shown in Figure 5c. The significant amount of fracture inside the fragments enhances energy dissipation. Intra-fragment fracture is more predominant in the block experiments and is promoted through the interaction of adjacent fragments and via initial failure and crack propagation through the body. The nature of the fracture network and the shape of the fragment reflects the complexity of these interactions and the initial fragmentation of the material. In particular, inter and trans-granular fracture contributes to secondary fragmentation inside the fragment. Compensating for these processes in numerical codes is difficult.

Finally, shown in Figure 5d, are melt features inside a fracture in plagioclase. Temperatures needed to cause melting are at least 1,400 K [2]. Work by Jaeger [20] estimates the mean temperature rise between a sliding heat source (i.e., generated through contacting surfaces) and semi-infinite body (i.e., the fracture surface) is given by:

$$\Delta T = \frac{4qf}{3k\sqrt{\pi}} \left(\frac{kL}{\rho cpV} \right)^{1/2} \tag{1}$$

where q is the heat flux (W/m^2), f is the fraction of heat flowing into the surface, k is thermal conductivity (Wm$^{-1\circ}$C), ρ is density (kg/m^3), cp is specific heat Jkg$^{-1\circ}$C^{-1}, L is the contact length (m), and V is the velocity of the sliding surface (m/s).

The heat source is produced from sliding surfaces and is estimated as the shear stress multiplied by the velocity. The shear stress is obtained from the normal yield stress of plagioclase (10^3 MPa [2]) and an assumed coefficient of friction (μ=0.4). All heat is assumed to be transferred through conduction under adiabatic conditions (i.e., no time for the heat to leave the system). A specific heat of 775 Jkg$^{-1\circ}$C^{-1} [2], thermal conductivity of 2.79 Wm$^{-1\circ}$C [2], density of 2700 kg/m^3 [2] and heat fraction of 0.5 are assumed. The total length of contact zone is taken as 20 μm. Allowing the velocity to vary, estimates of ΔT obtained from equation (1) are shown in Figure 6. Sliding velocities $>$ 5 m/s are able to achieve temperatures $\geq$ 1,000 K, and a sliding velocity of 16 m/s is able to reach 1,500 K. Works by Herget [21] and Bergstrom [22] found that the elastic strain energy released at failure was mostly converted to kinetic energy, with separation velocities of adjacent newly generated fracture surfaces of $>$10 m/s. From this work, surface velocities $>$ 5 m/s are realistic, and compounded with collisions from adjacent fragments, 1,400 K temperatures are achievable on the local micro-scale.

Formation mechanisms of sub 10 μm fragments are examined in Figure 7. All images are taken for the finer grained granitoid block. Fragments at this scale form through primarily brittle (Figure 7a) and ductile failure (Figure 7b). The melting and droplet formation of plagioclase (Figure 7c) to form a spheroid, and the agglomeration of melted plagioclase (Figure 7d) can also lead to fragment for-

mation. Combined, these highlight the contrasting micro-scale energy dissipation and fragment formation mechanisms during high speed impact.

5. Discussion and Implications

The dynamic fragmentation of gabbro and finer grained granitoid tiles, and coarser and finer grained granitoid blocks has been examined. Substantial intra-grain fragmentation is observed to be a common physical feature of the fragmentation process. This enhances energy dissipation. The generation of temperatures of the order of 1,400 K via frictional melting was observed to be a consequence of inter-granular fracture and micro-offset. These temperatures are realistic based on analytical work by Jaeger [20]. The generation of melt through frictional heating is important in earthquakes [23], faulting and melt vein formation during hypervelocity impact [24]. The implication here is that these temperatures are achievable under relatively moderate conditions. Combined, these highlight contrasting micro-scale energy dissipation and fragment formation mechanisms during high speed impact. Compensating for these processes in numerical codes is required.

Analysis of the rear of the target reveals the formation of cones for the finer grained granitoid block and the gabbro and granitoid tiles. No observable cones are present in the coarser grained blocks. The formation of cones in the targets is commonly observed in impact tests [19] and is attributed to Hertzian cone cracking. The trajectories of Hertzian cone fractures, defined here as the outer edge of the cone, are governed by the stress field in the body at impact [25] and this will follow the direction of maximum energy release [25]. For asymmetric loading in non-uniform stress fields, these trajectories do not necessarily correspond with the normal to the maximum tensile stress [25].

Next, the total volume contribution of the Hertzian cone with respect to the total volume of the target is considered. Assuming the cone has smooth sides and an apex angle of 27°, the ratio of the mass contained in the cone to the target mass is 0.01 for the 10 mm-thick tiles and 0.06 for the 55 mm thick blocks. These are less than 10% of the total ejected volume from the body. This indicates that another mode of fracture is primarily responsible for ejecting target material during these high-speed impact conditions. For the tile experiments, circumferential and radial through-cracking of larger pieces is believed to be responsible for ejection. Radial through-cracking of larger fragments is also believed to be responsible of larger target pieces for the finer grained granitoid block as well. Fracturing along grain boundaries and inherent flaws are responsible in the coarser grained blocks. The ejection of through-cracked fragments will contribute more mass, assuming similar fragment shape and equal densities, to the block than the tile experiments. For this reason, more percentage mass is ejected for the blocks; a result noted in Figure 3a.

Greater ejection sensitivity (i.e., power-law exponent) for larger grained materials is associated with increased larger-scale fracturing along, for example, grain boundaries. Secondary effects in the finer grained materials, such as comminution and associated energy dissipation via plastic deformation and heat, further limits the ejection sensitivity of these materials. Finer materials are less resistant to an increase in additional input energy due to increased strength [14]. Increased inter-granular fragmentation and enhanced grinding of surfaces also contributes to lower impact energy sensitivities for the total number of fragments for the finer grained materials ($\propto x^{0.11}$) compared to the larger ones ($\propto x^{1.28,0.67}$). The total number of fragments highlights the substantial sub-2mm fragmentation that oc-

curs under relatively low-speed impact conditions.

The consideration of fragmentation at sub-2 mm scales is important in the development and validation of numerical codes [26–28] and analytical models [29–33]. The objective of these models is to obtain scaling parameters (e.g., power-law coefficients) that can be applied to a variety of brittle materials. Percentile values (i.e., [0.1, 0.5, 0.9]) against fragment sizes (i.e., [x_{10}, x_{50}, x_{90}]) are fitted with lower-law curves in the form of:

$$f(x) = Cx^n \tag{2}$$

where $f(x)$ are the percentile fragment lengths (i.e., [x_{10}, x_{50}, x_{90}]), x is the percentile values (i.e., [0.1, 0.5, 0.9]), C is a scaling parameter, and n is the fractal dimension describing spread of the distributions and often the parameter of interest implemented in numerical codes. Shown in Figure 8 are values of the fractal dimension plotted against non-dimension impact energy. Here KE is the impact energy into the target, Y is yield strength of the material (Y_{gab}= 150 MPa [34], $Y_{GW,FG}$= 148 MPa [26], and Y_{CG}= 145 MPa [26],) and t is the target thickness. The term $KE/(Yt^3)$ will be referred to as KE^* in the text. Curve-fits are also applied to n vs. KE^* (Figure 8). The non-dimensional form of kinetic energy can include, for example, fracture toughness and density, as these are the material properties governing the fragmentation processes. Mechanical testing using a split-Hopkinson bar [35] are needed to provide more accurate values for yield strength and fracture toughness.

Fractal dimensions for Q_0 (greater values in the plot) are the greater than those associated with Q_3 (Figure 8). Fractal dimensions of approximately 2 to 3 are often reported for number distributions [36–38]. Target thickness was not consid-

ered in these previous studies. Values for the the fractal dimension intercept (c in cx^n) are greater the block experiments, with a larger values in both block and tile cases reported for the finer grained material. Higher fractal dimensions indicate that these materials are more crushed, as is expected based on other results. Reported fractal dimensions (1.5 to 1.7 for Gab, 1.3 to 1.5 for GW, 1.5 to 1.7 for CG, and 1.7 to 2.5 for FG) are lower than previous studies. This is likely due to the fact that fragment distributions from previous investigations are severely limited in the total number and size limitations of measured fragments, especially the smaller ones. The total number and size resolutions are factors that which can influence the fractal dimension and, more relevant to models predicting fragment sizes, the average fragment size. Automated microscopy results from these experiments indicate that fragment distributions mainly contain millions of fragments smaller than 10 μm, which contributes to discrepancies in previous experiments.

Fractal dimensions for the volume distribution of fragmentation sizes are smaller than the associated Q_0 values. Values of 0.3 to 0.5 for the gabbro material are in agreement with those by Lange et al. [34]. The fractal dimension for the GW experiments is larger 1.30 and suggests, as before, that significantly more crushing occurs. Fractal dimensions for the CG material is approximately 0.70 and for the FG 0.85. Again, these values reflect the increased crushing in the finer grained material and highlight the difference between the Q_0 and Q_3 fractal dimensions. Q_3-fractal dimensions are also less sensitive to KE^* than Q_0-fractal dimensions. Values for c-intercept of the volume distributions are not ordered like the number distributions, suggesting another level of interpretation is required in future studies when a more comprehensive data set is developed. Combined, these results highlight the differences between Q_3 and Q_0 fractal dimensions, suggesting

that percentile values (e.g., median fragment size) and fractal dimensions should be only considered for volume distributions. Extension of these considerations warrants future development in existing fragmentation models.

Automated microscopy of sub-200 μm fragments was performed to gain a better understanding of fragmentation mechanisms associated with the different experimental conditions. The large number of fragments contained within one sample of sub-200 μm fragments reflects the significant contribution of the finer fragments to the number distribution of particle sizes. Considerably more fines are produced in the tile and the finer grained block experiments than the coarser blocks. Enhanced intergranular fracture of the tiles and finer grained granitoid blocks promote the grinding of roughened fracture surfaces; especially for the granitoids. These trends are reflected in the circularity results.

Median values of automated microscopy, Q_0 and Q_3 measurements are compared with existing models by Grady [29], Glenn and Chudnovksy [30], Zhou et al. [31, 32] and Levy and Molinari [33] predicting average fragment size. Grady's model to calculate average fragment size assumes that local kinetic energy is converted to creating new surfaces. The average fragment size, s_{Grady}, according to Grady [29] is calculated as:

$$s_{\mathrm{Grady}} = \left(\frac{48 G_c}{\rho \dot{\epsilon}^2} \right)^{1/3} \tag{3}$$

where ρ is the material density (kg/m^3), $\dot{\epsilon}$ is strain rate (s^{-1}), and G_c is the fracture energy (J/m^2).

Glenn and Chudnovksy [30] modified Grady's theory to include a strain energy term for lower strain rates. They assumed that stored strain energy and local

kinetic energy are converted to fracture energy during fragmentation and propose that the average fragment size be calculated from:

$$\mathrm{s_{GC}} = 4\sqrt{\frac{3}{\alpha}} sinh\left(\frac{\phi}{3}\right) \tag{4}$$

where

$$\phi = sinh^{-1}\left[\beta\left(\frac{3}{\alpha}\right)^{3/2}\right] \tag{5}$$

and

$$\alpha = \frac{3\sigma_c^2}{\rho E \dot{\epsilon}^2} \tag{6}$$

$$\beta = \frac{3G_c}{2\rho\dot{\epsilon}^2} \tag{7}$$

where E is Young's modulus (Pa) and σ_c is the compressive strength of the material before failure (Pa).

Zhou et al. [31, 32] proposed the strain-rate dependent fragment size as:

$$\mathrm{s_{Zhou}} = \frac{4.5EG_c}{\sigma_c^2}\left[1 + 0.77\left(\frac{\dot{\epsilon}}{c\sigma_c^3/E^2G_c}\right)^{1/4} + 5.4\left(\frac{\dot{\epsilon}}{c\sigma_c^3/E^2G_c}\right)^{3/4}\right]^{-1} \tag{8}$$

where c is the longitudinal speed of sound (m/s) in the material given by:

$$c = \sqrt{\frac{E}{\rho}} \tag{9}$$

Levy and Molinari [33] proposed the average fragment size be calculated as:

$$\mathrm{s_{LM}} = t_0 C_{eff} \frac{3}{1 + 4.5\left(Et_0/\mu_{init}\right)^{2/3}\dot{\epsilon}^{2/3}} \tag{10}$$

where C_{eff} is effective longitudinal speed of sound and given as:

$$C_{eff} = c\left(\frac{2}{a+1}\right)^{1/2}\left(\frac{\sigma_{c,min}}{\mu_{init}}\right)^{1/5} \tag{11}$$

where c is the wave speed, $\sigma_{c,min}$ is the strength of the weakest link in a probability distribution of defects, μ_{init} is the average strength, a is a scaling parameter depending on what type of distribution is chosen (e.g., Wiebull, Gaussian), and t_0 is a characteristic time (s) defined by Zhou et al. [32] as:

$$t_0 = \frac{EG_c}{c\sigma_c^2} \tag{12}$$

Shown in Figure 9 is the theoretical fragment size plotted against strain rate and the median values of experimental results. Granite is assumed as the material for comparison. Values are taken as: ρ=2,700 kg/m^3, G_c= 70 J/m^2 [26], E= 80 GPa [26], σ_c=240 MPa [39], μ_{init}=σ_c/2 (based on ratios used by Levy and Molinari [33]), and a=0.65 [33]. Strain rate is estimated as the impact velocity over the target thickness and is varied. Values for the median volume distributions (highlighted as Q_3 in figure) are in range of those predicted by Grady [29]. Values for the median Q_0 fragment size are reasonably well predicted by the Zhou et al. [32] and Levy and Molinari [33] models. Mean values (not shown) are approximately an order of magnitude larger, and, hence, are not reasonably predicted by these models. Values obtained from automated microscopy results (highlighted in figure) are approximately an order of magnitude smaller than those predicted by theory. Combined, these results reflect the two distinct fragment-forming mechanisms during impact testing of natural geological materials. One mechanism is based on an energy consideration of the bulk material, which produces the larger

fragment size, and the other is associated with micro-scale comminution, which produces sub-10 μm fines.

6. Concluding Remarks

The dynamic fragmentation of gabbro and granitoid tiles, and coarser and finer grained granitoid blocks has been examined. Intra-grain fragmentation and inter-granular frictional melting were observed to be common features of the fragmentation process. Consideration of analytical models by Jaeger [20] indicate that high temperatures are achievable under relatively moderate conditions.

Circumferential and radial-through cracking, and fracturing along inherent flaws (coarser blocks) was the primary mode of material ejection from the target. Increased inter-granular fragmentation and enhanced surface grinding contributed to lower impact energy sensitivities for material removal. Sub 10 μm fine production does not occur as much in the coarser grained granitoid block and is attributed to common fracture along grain boundaries in this material.

Median values of the number-based sub-10 μm fine, and the number- and volume-based 10 μm to 2 mm fragments were compared with existing theoretical models predicting dominant fragment size. The simplistic model proposed by Grady [29] predicts reasonably well the median fragment size for the volume-based distribution. The more complex models [31–33] are able to predict reasonably well median values for Q_0. Ultra-fine production was not predictable. The consideration of fractal dimensions for a proposed non-dimensional kinetic energy term, KE^*, further highlighted differences among the number- and volume-based descriptions of the fragmentation process. In the future, it is suggested that volume-based descriptions of median values should be considered in the de-

velopment of analytical and numerical models of the dynamic fragmentation of ceramic materials. These results suggest there are two distinct fragment-forming mechanisms during the impact testing of granitoid materials. One mechanism is based on an energy consideration of the bulk material, which produces the larger fragment size, and the other is associated with micro-scale comminution, which produces sub-10 μm fines.

Important length scales and physical mechanisms identified here can be used to improve and validate multi-scale models of natural ceramic fragmentation. Combined with implementation of damage laws [40], and the use of cohesive elements [41, 42] in finite element method-based techniques [41–43], and the recent advances in atomistic modelling [44], a more detailed characterization of energy conversion (e.g., strain, plastic, fracture, kinetic) can be obtained. A greater understanding of important fragmentation length scales and physical interpretations of fragmentation mechanisms will lead to improved engineering of ceramics in mining and armour applications.

Acknowledgements

This work was supported by a Natural Sciences and Engineering Research Council (NSERC) PGS-D scholarship to JDH and funding from NSERC, the Canada Research Chairs program and the Canada Foundation for Innovation to JGS. Planetary and Space Science Centre contribution 69. The authors would like to thank the effort and contribution during the experimental phase of the study of Yannick Boehrer, Gregory Vincent, David Bluntzer and Philippe Baumann at ISL. The authors would also like to thank the technical support of Alon Vaisman during measurements at Malvern Instruments and Suporn Boonsue for SEM op-

eration. Karen Shea is thanked for her continued support and preparation of this manuscript.

[1] G. Hu, H. Otaki, M. Lin, An index of the tensile strength of brittle particles, Minerals Engineering 14 (10) (2001) 1199 – 1211. doi:10.1016/S0892-6875(01)00137-6.
URL http://www.sciencedirect.com/science/article/pii/S0892687501001

[2] J. G. Spray, Frictional melting processes in planetary materials: From hypervelocity impact to earthquakes, Annual Review of Earth and Planetary Sciences 38 (1) (2010) 221–254.

[3] J. S. Chester, F. M. Chester, A. K. Kronenberg, Fracture surface energy of the punchbowl fault, san andreas system, Nature 437 (2005) 133–136.

[4] R. Buttner, P. Dellino, H. Raue, I. Sonder, B. Zimanowski, Stress-induced brittle fragmentation of magmatic melts: Theory and experiments, Journal of Geophysical Research B: Solid Earth 111 (8).

[5] D. Tromans, Mineral comminution: Energy efficiency considerations, Minerals Engineering 21 (8) (2008) 613 – 620. doi:DOI: 10.1016/j.mineng.2007.12.003.

[6] D. W. Fuerstenau, A. Z. M. Abouzeid, The energy efficiency of ball milling in comminution, International Journal of Mineral Processing 67 (1-4) (2002) 161 – 185. doi:DOI: 10.1016/S0301-7516(02)00039-X.

[7] D. Tromans, J. Meech, Fracture toughness and surface energies of minerals: Theoretical estimates for oxides, sulphides, silicates and halides, Minerals Engineering 15 (12) (2002) 1027–1041.

[8] D. Tromans, J. Meech, Fracture toughness and surface energies of covalent minerals: Theoretical estimates, Minerals Engineering 17 (1) (2004) 1–15.

[9] J. Hagan, Impossibility of fragmenting small particles: brittle-ductile transition, Journal of Materials Science 16 (1981) 2909–2911, 10.1007/BF02402857.
URL http://dx.doi.org/10.1007/BF02402857

[10] K. Schoenert, Role of fracture physics in understanding comminution phenomena., Trans Soc Min Eng AIME 252 (1) (1972) 21–26.

[11] C. Koch, Synthesis of nanostructured materials by mechanical milling: Problems and opportunities, Nanostructured Materials 9 (1-8) (1997) 13–22.

[12] V. Boldyrev, S. Pavlov, E. Goldberg, Interrelation between fine grinding and mechanical activation, International Journal of Mineral Processing 44-45 (SPEC. ISS.) (1996) 181–185.

[13] C. Knieke, M. Sommer, W. Peukert, Identifying the apparent and true grinding limit, Powder Technology 195 (1) (2009) 25 – 30.

[14] History of the Strength of Materials, McGraw-Hill, London, 1953, p. 58.

[15] Malvern Instruments, Parsum ipp 70-s, http://www.malvern.com.

[16] Malvern Instruments, Morphologi g3, http://www.malvern.com.

[17] International Organization for Standardization (ISO) 9276-2:2001, Representation of results of particle size analysis – part 2: Calculation of average particle sizes/diameters and moments from particle size distributions.

[18] F. Kick, Das gesetz des proportionalen widerstandes und seine anwendung, Arthur Felix, Leipzig.

[19] J. D. Hogan, J. G. Spray, R. J. Rogers, S. Boonsue, G. Vincent, M. Schneider, Micro-scale energy dissipation mechanisms during dynamic fracture in natural polyphase ceramic blocks, International Journal of Impact Engineering 38 (12) (2011) 931 – 939. doi:10.1016/j.ijimpeng.2011.06.004.
URL http://www.sciencedirect.com/science/article/pii/S0734743X11001

[20] J. C. Jaeger, Moving sources of heat and the temperature at sliding surfaces, Journal Proceedings of the Society of New South Whales 76 (1942) 205 – 224.

[21] G. Herget, Stresses in Rock, Balkema,Rotterdam, 1988.

[22] C. H. Bergstrom, Energy and size distribution aspects of single particle crushing., Proceedings of the 5th Symposium on Rock Mechanics Rock Mechanics (1963) p 155–172.

[23] B. N. Cox, H. Gao, D. Gross, D. Rittel, Modern topics and challenges in dynamic fracture, Journal of the Mechanics and Physics of Solids 53 (3) (2005) 565 – 596. doi:10.1016/j.jmps.2004.09.002.
URL http://www.sciencedirect.com/science/article/pii/S0022509604001

[24] M. B. Biren, J. G. Spray, Shock veins in the central uplift of the manicouagan impact structure: Context and genesis, Earth and Planetary Science Letters 303 (34) (2011) 310 – 322. doi:10.1016/j.epsl.2011.01.003.

[25] C. Kocer, R. E. Collins, Angle of hertzian cone cracks, Journal of the American Ceramic Society.

[26] H. Ai, T. Ahrens, Simulation of dynamic response of granite: A numerical approach of shock-induced damage beneath impact craters, International Journal of Impact Engineering 33 (1-12) (2006) 1 – 10, hypervelocity Impact Proceedings of the 2005 Symposium.

[27] S. Maiti, K. Rangaswamy, P. H. Geubelle, Mesoscale analysis of dynamic fragmentation of ceramics under tension, Acta Materialia 53 (3) (2005) 823 – 834. doi:10.1016/j.actamat.2004.10.034.
URL http://www.sciencedirect.com/science/article/pii/S1359645404006

[28] M. Jutzi, P. Michel, W. Benz, D. C. Richardson, Fragment properties at the catastrophic disruption threshold: The effect of the parent bodys internal structure, Icarus 207 (1) (2010) 54 – 65. doi:10.1016/j.icarus.2009.11.016.
URL http://www.sciencedirect.com/science/article/pii/S0019103509004

[29] D. E. Grady, Length scales and size distributions in dynamic fragmentation, International Journal of Fracture 163 (1–2) (2009) 85–99.

[30] L. A. Glenn, A. Chudnovsky, Strain and energy effects on dynamic fragmentation, Journal of Applied Physics 59 (4) (1986) 1379 –1380.

[31] F. Zhou, J. F. Molinari, K. Ramesh, Analysis of the brittle fragmentation of an expanding ring, Computational Materials Science 37 (1-2) (2006) 74 – 85.

[32] F. Zhou, J. F. Molinari, K. T. Ramesh, Effects of material properties on the fragmentation of brittle materials, International Journal of Fracture 139 (2006) 169–196.

[33] S. Levy, J. Molinari, Dynamic fragmentation of ceramics, signature of defects and scaling of fragment sizes, Journal of the Mechanics and Physics of Solids 58 (1) (2010) 12 – 26.

[34] M. A. Lange, T. J. Ahrens, M. B. Boslough, Impact cratering and spall failure of gabbro, Icarus 58 (3) (1984) 383 – 395. doi:10.1016/0019-1035(84)90084-8.
URL http://www.sciencedirect.com/science/article/pii/00191035849008

[35] J. Kimberley, K. T. Ramseh, O. S. Barnouin, Visualization of the failure of quartz under quasi-static and dynamic compression, Journal Of Geophysical Research 115 (2010) B02807.

[36] C. G. Sammis, G. C. P. King, Mechanical origin of power law scaling in fault zone rock, Geophysical Research Letters 34 (L04312). doi:doi:10.1029/2006GL028548.

[37] J. D. Hogan, R. J. Rogers, J. G. Spray, S. Boonsue, Dynamic fragmentation of granite for impact energies of 628 j, Engineering Fracture Mechanics (0) (2011) –. doi:10.1016/j.engfracmech.2011.10.006.
URL http://www.sciencedirect.com/science/article/pii/S0013794411003

[38] A. C. Palmer, T. J. O. Sanderson, Fractal crushing of ice and brittle solids, Proc. R. Soc. Lond. A 433 (1889) (1991) 469–477. doi:doi:10.1098/rspa.1991.0060.

[39] H.-A. Ai, Dynamic tensile strength of terrestrial rocks and application to impact cratering, Meteoritics and Planetary Science 39 (1 February 2004) 233–246(14).

[40] V. V. Kharchenko, A. L. Maistrenko, A. I. Babutskii, E. A. Kondryakov, Impact deformation and fracture mechanisms of plates of brittle materials, Strength of Materials 34 (2002) 269–272, 10.1023/A:1016270617063.
URL http://dx.doi.org/10.1023/A:1016270617063

[41] G. Camacho, M. Ortiz, Computational modelling of impact damage in brittle materials, International Journal of Solids and Structures 33 (2022) (1996) 2899 – 2938. doi:10.1016/0020-7683(95)00255-3.
URL http://www.sciencedirect.com/science/article/pii/00207683950025

[42] X.-P. Xu, A. Needleman, Numerical simulations of fast crack growth in brittle solids, Journal of the Mechanics and Physics of Solids 42 (9) (1994) 1397 – 1434. doi:10.1016/0022-5096(94)90003-5.
URL http://www.sciencedirect.com/science/article/pii/00225096949000

[43] G. Barenblatt, The mathematical theory of equilibrium cracks in brittle fracture, Vol. 7 of Advances in Applied Mechanics, Elsevier, 1962, pp. 55 – 129. doi:10.1016/S0065-2156(08)70121-2.
URL http://www.sciencedirect.com/science/article/pii/S0065215608701

[44] M. Marder, S. Gross, Origin of crack tip instabilities, Journal of the Mechanics and Physics of Solids 43 (1) (1995) 1 – 48. doi:10.1016/0022-5096(94)00060-I.
URL http://www.sciencedirect.com/science/article/pii/00225096940006

List of Figures

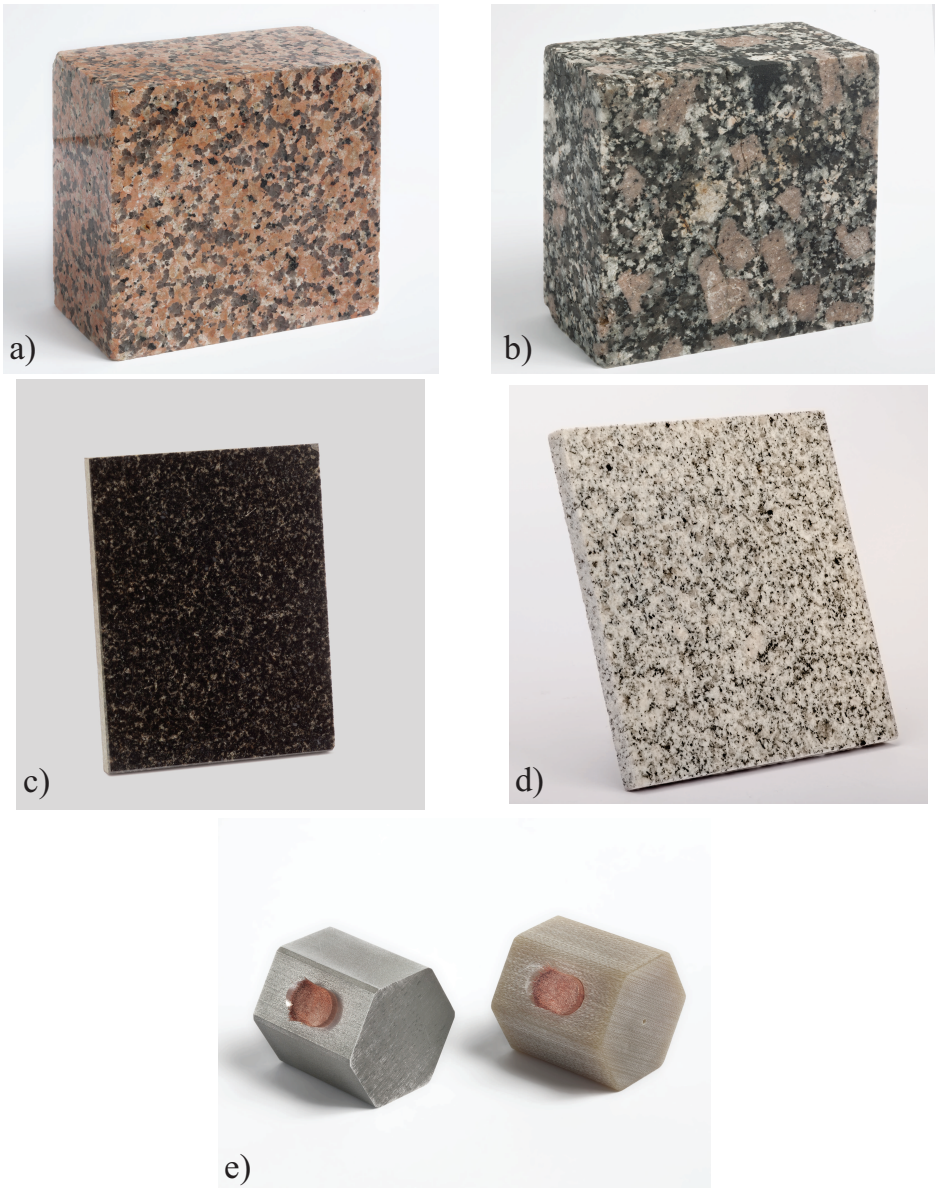

Fig. 1: Photographs of the target material: (a) finer grained granitoid and (b) coarser-grained granitoid, (c) gabbro tile, (d) granitoid tile and (e) projectiles (aluminum on left and composite on right). The tiles are 10 mm thick, the blocks are 55 mm thick and the projectiles are 32 mm in length.

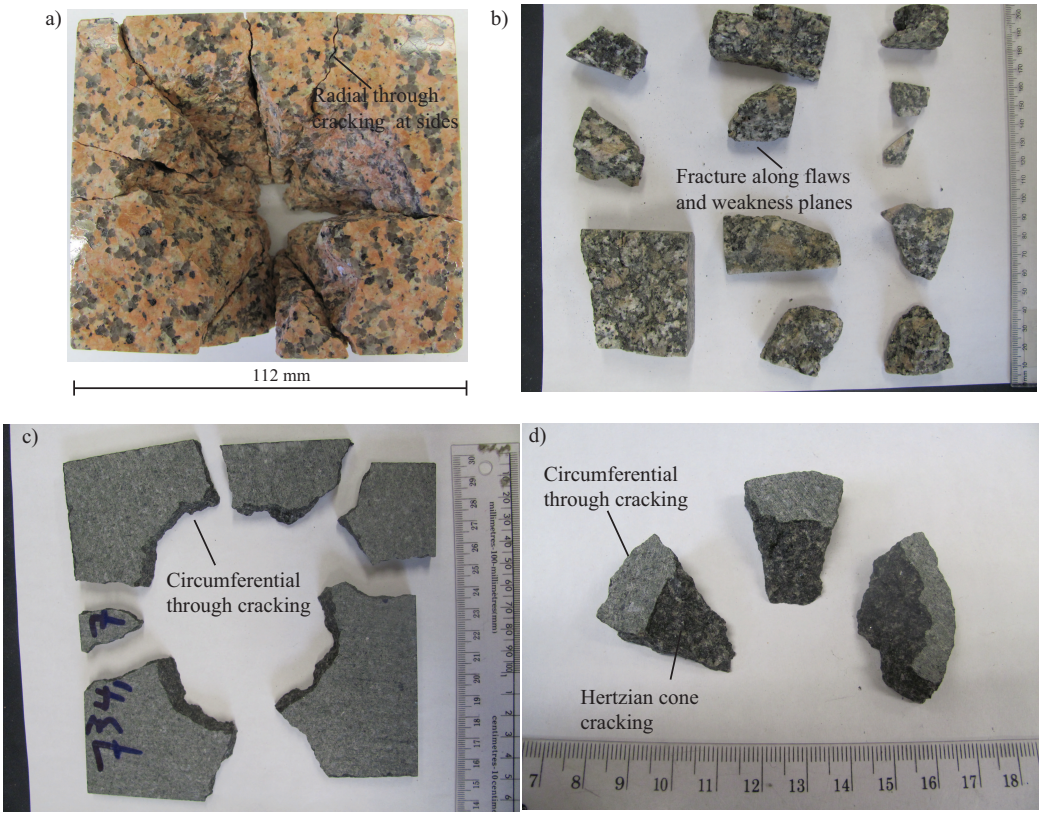

Fig. 2: (a) Rear of the target of the finer grained material at 3,730 J showing Hertzian cone cracking, (b) the residual coarser grained target at 3,040 J indicating no Hertzian cone cracking, and (c,d) evidence of through-circumferential and radial cracking and Hertzian cone cracking in the gabbro tile at 305 J.

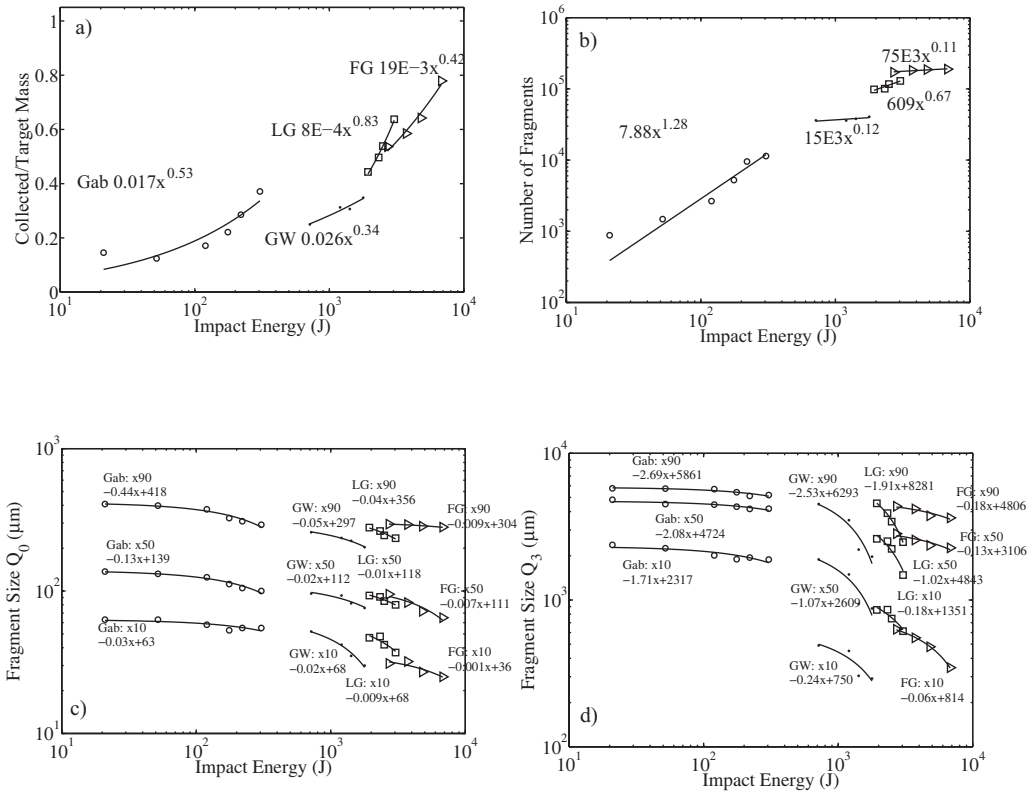

Fig. 3: (a) The ratio of ejected mass and original target mass, (b) number of fragments measured with Parsum probe versus impact energy, and x_{10}, x_{50}, x_{90} for (c) number distribution, and (d) volume distribution of fragments. Abbreviations: Gab: gabbro tiles, GW: granitoid tiles, FG: finer grained granitoid block, and LG: coarser grained granitoid block.

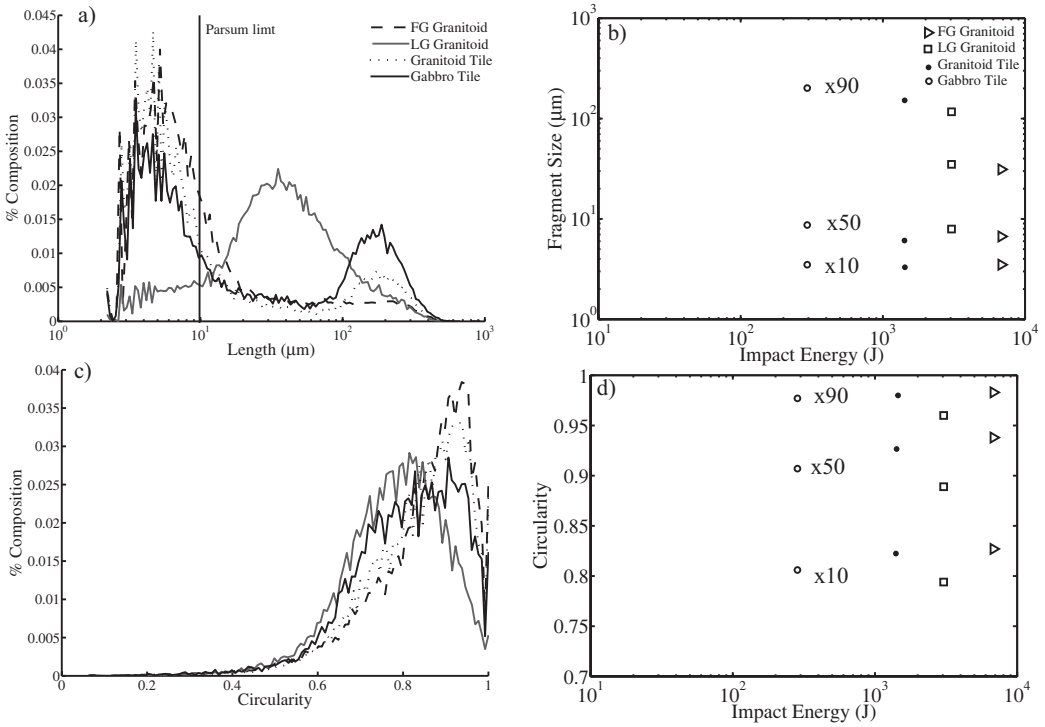

Fig. 4: Histogram distributions and corresponding x_{10}, x_{50}, x_{90} values for (a,b) fragment size, (c,d) circularity, (e,f) mean intensity, (g,h) standard deviation of intensity.

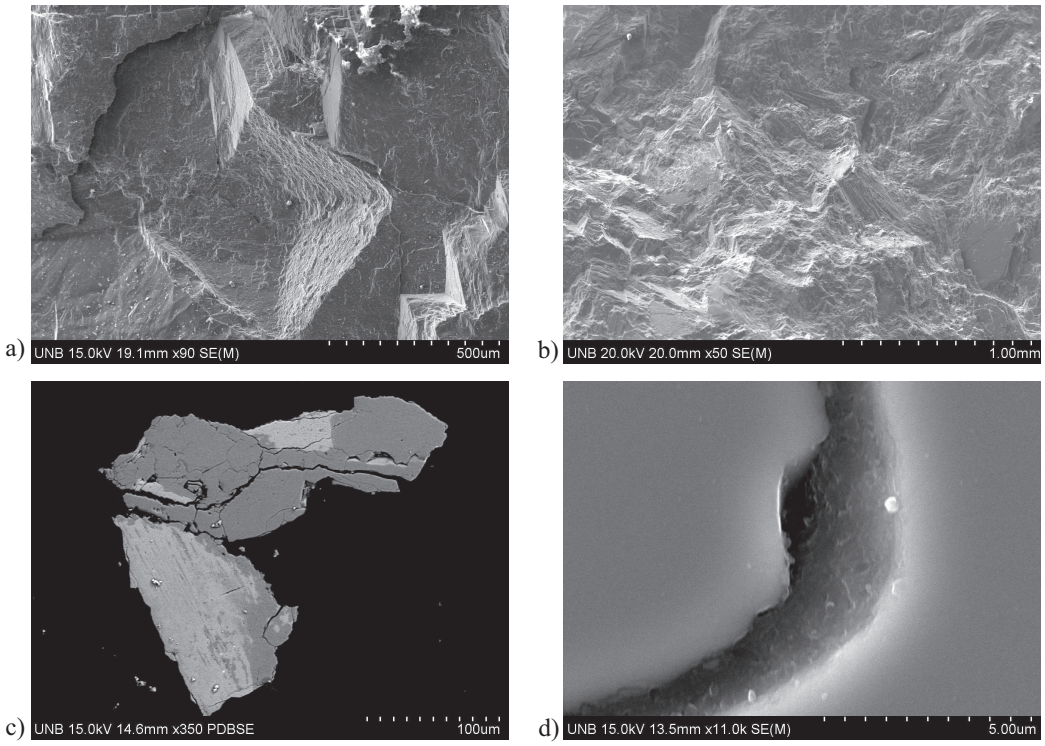

Fig. 5: SEM images: fracture surface in (a) finer grained granitoid block and (b) gabbro tile, (c) intra-fragment fracture and (d) melting evidence during fracture in the granitoid block.

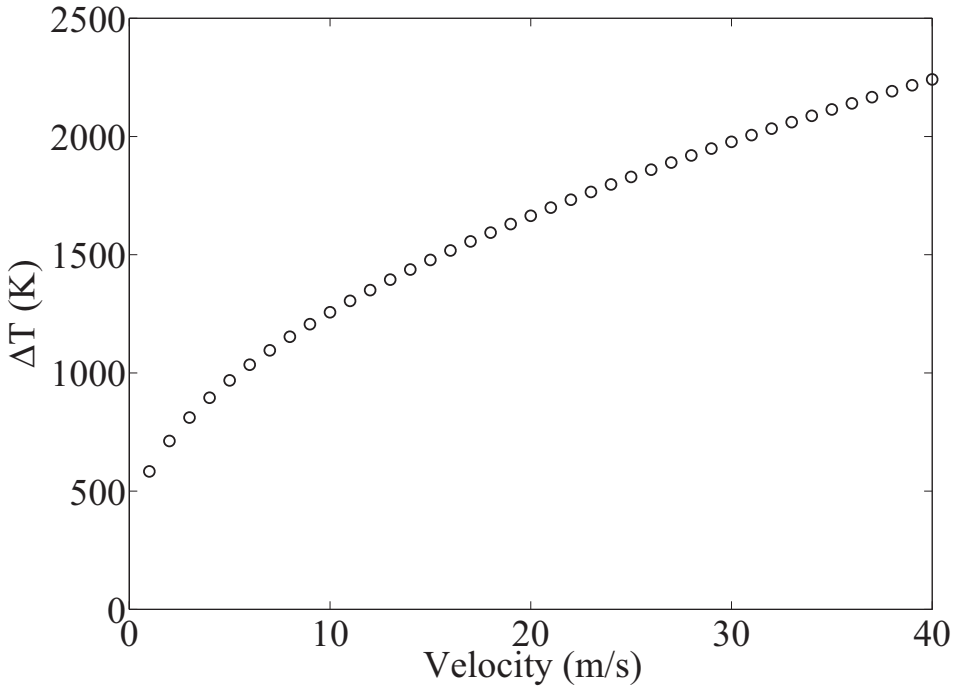

Fig. 6: Estimate of mean temperature rise (K) according to Jaeger [20] with sliding surface velocity.

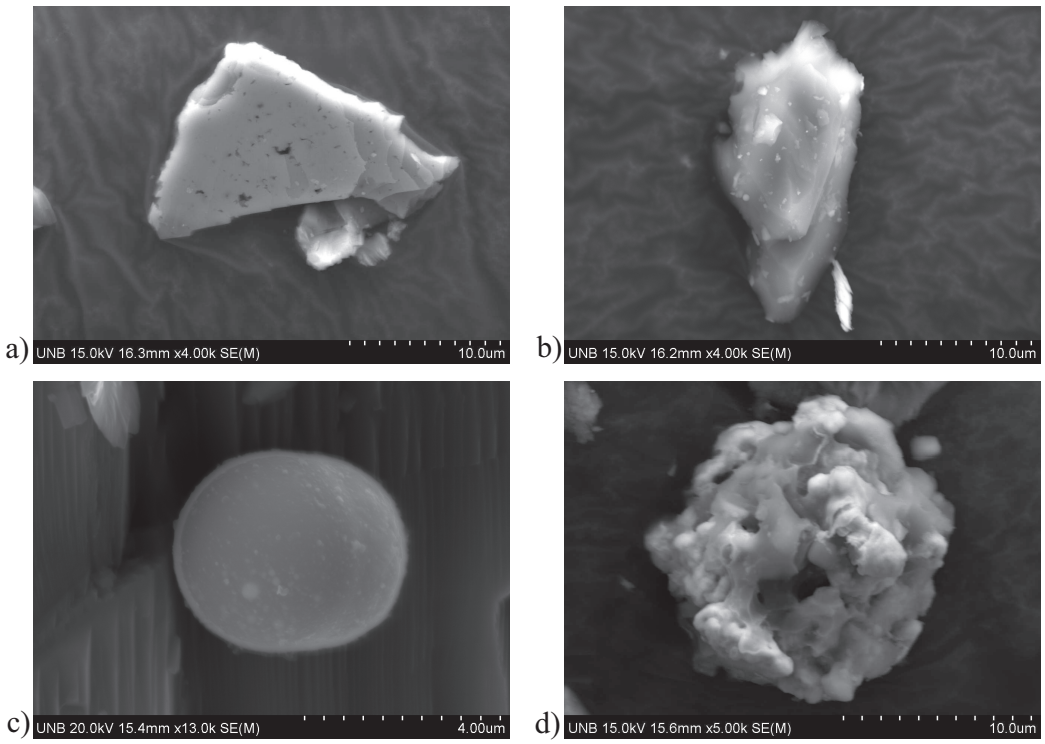

Fig. 7: SEM images of sub-10μm fragments formed via (a) intergranular fracture and (b) through plastic deformation, and (c) melting and re-solidification of a spheroid and (d) agglomeration of melt.

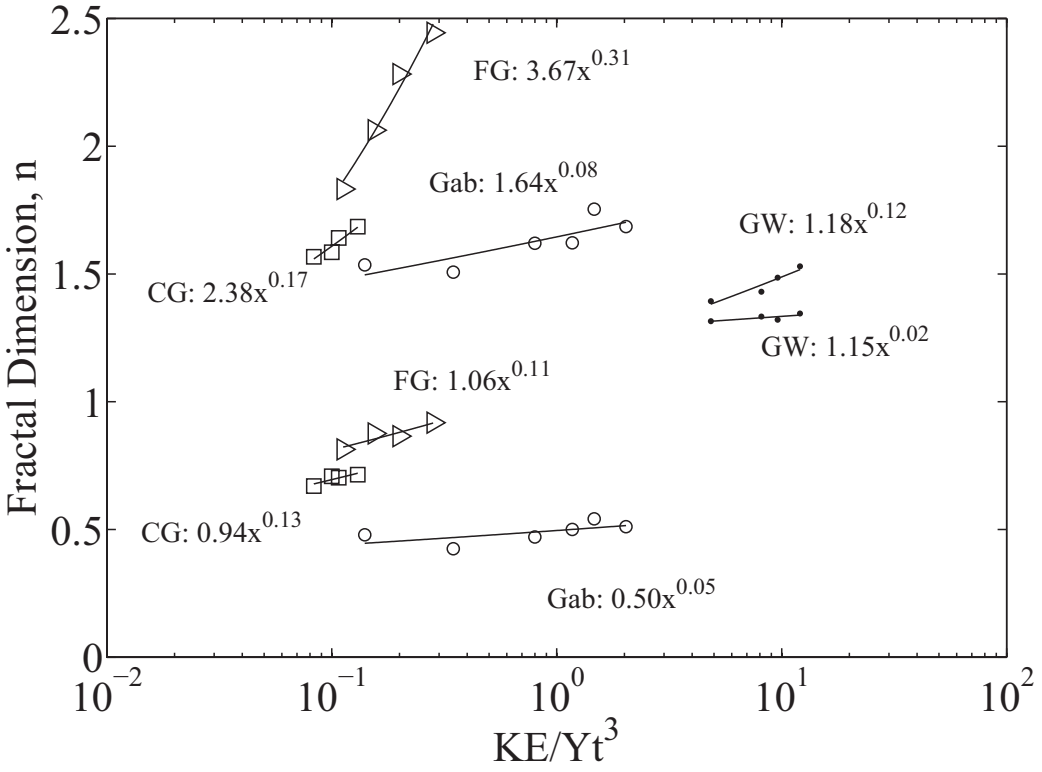

Fig. 8: Fractal dimensions of the volume and number based fragment size distributions plotted against impact energy. Q_0 values greater than Q_3. Gab: gabbro tiles, GW: granitoid tiles, FG: finer grained granitoid blocks, and CG: coarser grained granitoid blocks.

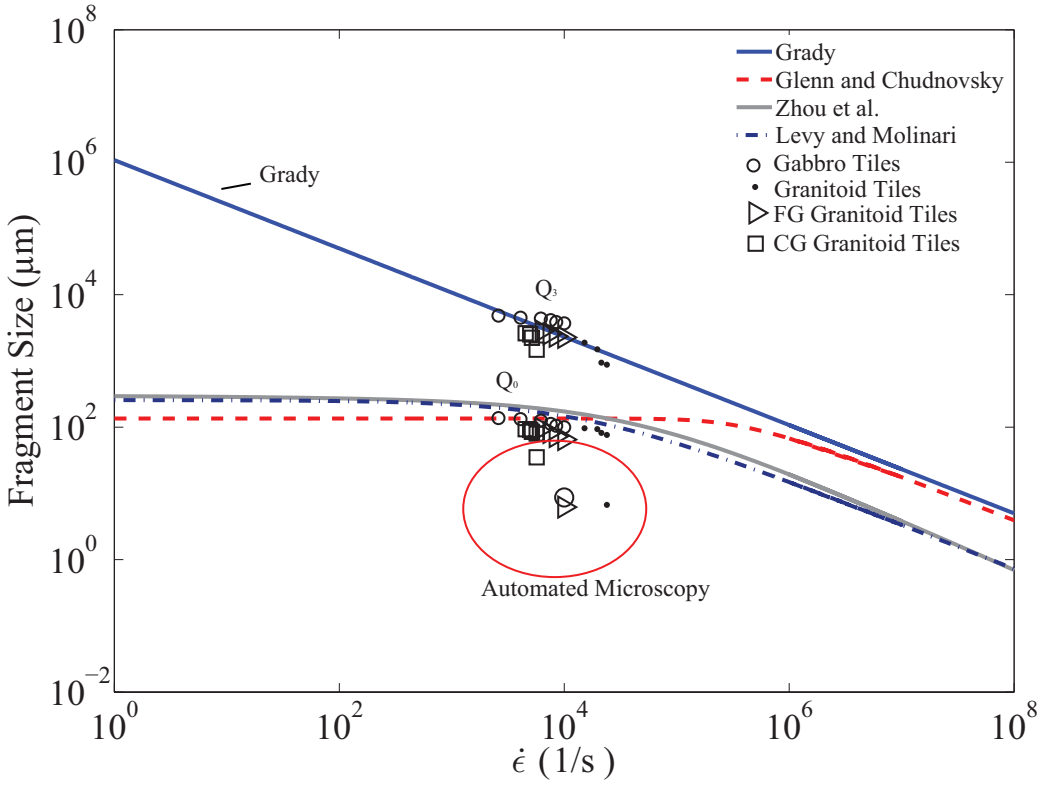

Fig. 9: A comparison of experimental fragment sizes with theoretical predictions.

7. Nomenclature

a	Scaling parameter for the Levy and Molinari [33] prediction of fragment size
c	Longitudinal wave speed, m/s
cp	specific heat Jkg$^{-1\circ}$C^{-1}
C	Proportionality constant
E	Young's modulus, Pa
f	fraction of heat flowing into the surface
G_c	Fracture energy, J/m^2
k	thermal conductivity (Wm$^{-1\circ}$C)
KE	Kinetic energy, J
K_c	Fracture toughness, Pa$\sqrt{m}$
n	Fractal dimension
L	contact length (m)
q	heat flux (W/m^2)
s_{GC}	Average fragment size according to Glenn and Chudnovksy [30], m
s_{Grady}	Average fragment size according to Grady [29], m
s_{Zhou}	Average fragment size according to Zhou [31, 32], m
s_{LM}	Average fragment size according to Levy and Molinari [33], m
s_{GC}	Average fragment size according to Glenn and Chudnovksy [30], m
t	Thickness of target, m
t_0	Characteristic time defined by Zhou [31, 32], s
x_i	ith percentile
v	Impact velocity, m/s
V	velocity of the sliding surface (m/s)
Y_{yield}	Yield stress, Pa

$\dot{\epsilon}$	Strain rate, s^{-1}
μ_{init}	Average strength for the Levy and Molinari [33] prediction of fragment size, Pa
ν	Poisson ratio
ρ	Material density, kg/m^3
σ_c	Compressive strength of the material before failure, Pa
$\sigma_{c,min}$	Strength of the weakest link in a probability distribution of defects [33], Pa
σ_{hel}	Hugoniot elastic limit, Pa